The Astrophysical Journal, 772:71 (12pp), 2013 July 20 doi:10.1088/0004-637X/772/1/71

PROMINENCE PLASMA DIAGNOSTICS THROUGH EXTREME-ULTRAVIOLET ABSORPTION

E. Landi[1] and F. Reale[2]

[1] Department of Atmospheric, Oceanic and Space Sciences, University of Michigan, Ann Arbor, MI 48109, USA

[2] Dipartimento di Fisica e Chimica, Università di Palermo, Piazza del Parlamento 1, I-90134 Palermo, Italy

Received 2012 September 13; accepted 2013 June 5; published 2013 July 8

ABSTRACT

In this paper, we introduce a new diagnostic technique that uses EUV and UV absorption to determine the electron temperature and column emission measure, as well as the He/H relative abundance of the absorbing plasma. If a realistic assumption on the geometry of the latter can be made and a spectral code such as CHIANTI is used, then this technique can also yield the absorbing plasma hydrogen and electron density. This technique capitalizes on the absorption properties of hydrogen and helium at different wavelength ranges and temperature regimes. Several cases where this technique can be successfully applied are described. This technique works best when the absorbing plasma is hotter than 15,000 K. We demonstrate this technique on AIA observations of plasma absorption during a coronal mass ejection eruption. This technique can be easily applied to existing observations of prominences and cold plasmas in the Sun from almost all space missions devoted to the study of the solar atmosphere, which we list.

Key words: Sun: coronal mass ejections (CMEs) – Sun: filaments, prominences – Sun: UV radiation

Online-only material: color figures

1. INTRODUCTION

Prominences are a common feature of both the active and the quiet solar corona. They consist of large structures of plasma in the solar inner atmosphere maintained by a strong and complex magnetic field configuration, which is able to keep their very low temperature plasma (i.e., 10,000 K or less in their cores) separated from the multimillion solar corona that surrounds them. Such a magnetic field configuration may last as long as several solar rotations, but it can also be destabilized; in the latter cases, the prominence erupts and is ejected in the interplanetary space, forming the core of a coronal mass ejection (CME).

Since prominence plasmas are very cold, they can be observed in the visible through H I emission (outside the limb) or as dark features called filaments (inside the disk); absorption features are also a common prominence manifestation at shorter wavelengths. Visible observations of prominences have been carried out since the 1800s, and a large body of literature has been produced that studies their morphology, evolution, and their physical and dynamical properties. Reviews of these results can be found, for example, in Labrosse et al. (2010), Tandberg-Hanssen (1995) and references therein.

One of the main open questions in prominence science is the role played by these structures in the initiation and propagation of CMEs. In fact, prominences are present in a sizeable fraction of all CMEs launched by the Sun, and prominence plasma has also been observed in-situ by mass spectrometers carried by the *ACE*, *Ulysses*, and *STEREO* satellites. In-situ measurements of prominence plasma properties such as element and charge state composition can provide very important information on the original prominence element composition: despite being largely unknown, plasma composition can provide information both on the origin of the prominence plasma itself, and on the heating and cooling processes experienced by the prominence during the early phases of CME acceleration. For example, Landi et al. (2010) provided evidence that erupting prominences are heated to temperatures in excess of 200,000 K in the earliest phases of CME initiation; still, Lepri & Zurbuchen (2010) and Gilbert et al. (2012) showed that cold prominence material ($T \simeq$ 40–70,000 K, where singly ionized C, O, and Fe were present) is common in interplanetary CMEs. Understanding the thermal history of an erupting CME may shed light on the unknown processes that create a CME in the first place. Coordinated studies of in-situ measurements of plasma element and charge state composition and remote-sensing determinations of plasma temperature and density during acceleration in the same CME event can provide vital constraints to CME initiation models, as shown by Gruesbeck et al. (2011, 2012) and Landi et al. (2012).

Measuring the physical properties of prominences has proven to be difficult. In the visible range, it is necessary to address radiative transfer of the prominence emission, so that complex models are necessary to reproduce the observations and describe the physical properties of prominence plasmas. The launch of satellite-borne X-ray, EUV, and UV instrumentation has opened a new window in prominence science that has enabled the study of the little known prominence-corona transition region and its properties on one side, and EUV and X-ray absorption on the other. The first to utilize EUV absorption to study the physical properties of prominences were Orrall & Schmahl (1976) using *Skylab* observations. This study paved the way to a large number of applications of absorption diagnostics of prominences as well as other plasmas. For example, Batchelor & Schmahl (1994) extended absorption analysis to X-ray observations of several solar structures, while Kucera et al. (1998) used EUV absorption observations from the Coronal Diagnostic Spectrometer (CDS) on board *Solar and Heliospheric Observatory* (*SOHO*) to determine the prominence column density and filling factor. Golub et al. (1999) were the first to apply absorption diagnostic techniques to *Transition Region and Coronal Explorer* (*TRACE*) data, determining the prominence plasma column density and electron density. The different EUV absorption properties of He and H were noted by Kucera et al. (1998), who proposed them as a tool to determine the He/H abundances. Since the beginning of the *SOHO* era, a large number of authors used CDS, SUMER, and *TRACE* observations to determine the plasma electron and hydrogen densities in prominences, their filling factor, their He/H abundance ratio and their mass as a function of time. An

excellent review of absorption diagnostic results can be found in Gilbert et al. (2011).

In this work, we focus on the wavelength and temperature dependence of EUV absorption. Capitalizing on the fact that the absorption coefficient of a plasma depends on its electron temperature when the latter exceeds $\simeq$15,000 K, we develop a novel technique to determine the electron temperature of an absorbing plasma. This technique can be applied to observations from both high-resolution spectrometers and narrow-band imagers from all past and current space missions such as *SOHO*, *TRACE*, *STEREO*, *Hinode*, SWAP, and *SDO*, as well as future missions such as Solar-C, Solar Probe, and Solar Orbiter. The principle of this diagnostic technique (and its limitations) is described in Section 2, and a few cases where it can be applied are outlined in Section 3. We demonstrate the technique on Atmospheric Imaging Assembly (AIA) observations of a CME event in Section 4, and discuss the results in Section 5. Section 6 suggests future applications to existing data.

2. THE DIAGNOSTIC TECHNIQUE

The diagnostic technique that we have developed relies on the EUV absorption properties of prominence material through bound-free transitions. Thus, it is useful to recall a few basic properties of bound-free EUV absorption.

2.1. The Absorption Coefficient

The intensity $F_{\rm obs}$ emerging from a non-emitting slab with thickness S made of material that absorbs the incident radiation $F_{\rm inc}$ emitted by a source located behind the slab is given by

$$F_{\rm obs} = F_{\rm inc} e^{-\tau}, \tag{1}$$

where

$$\tau = \int_0^S n_{\rm abs} k_{\rm abs} dl, \tag{2}$$

where τ is the optical thickness, $k_{\rm abs}$ is the absorption coefficient, and $n_{\rm abs}$ is the total number density of absorbers along the radiation path. In realistic cases, the absorbing plasma is made of several different elements, each distributed in a range of ionization stages which depend on the physical properties of the absorbing plasma itself. In this case, assuming that each ion in the absorbing plasma interacts with the incident radiation independently from the others, the optical thickness τ can be expressed as

$$\tau = \int_0^S \left[\sum_X \sum_m n(X^{m+}) k_{X,m} \right] dl, \tag{3}$$

where $n(X^{m+})$ is the density of ions $m+$ of the element X present along the line of sight, each characterized by its own absorption coefficient $k_{X,m}$, related to the absorption cross section (in cm^2). In EUV observations of solar prominences (i.e., between $\approx$100 Å and $\approx$1000 Å), absorption is dominated by H and He, which are the most abundant components of solar plasmas. Thus, a combination of H I, He I, and He II atoms and ions will be present along the line of sight, so that Equation (3) can be simplified to

$$\tau = \int_0^S n_{\rm H} k_{\rm eff} dl \tag{4}$$

$$k_{\rm eff} = f({\rm H\,I}, T) k_{\rm H\,I} + A_{\rm He} [f({\rm He\,I}, T) k_{\rm He\,I} + f({\rm He\,II}, T) k_{\rm He\,II}], \tag{5}$$

where the functions f indicate the fractional abundances of H I, He I, and He II (for example, for He II $f({\rm He\,II}, T) = n({\rm He\,II})/n({\rm He})$), which depend on the plasma electron temperature, and $k_{\rm (ion)}$ is the individual absorption cross sections of each of these three species. $A_{\rm He} = n({\rm He})/n({\rm H})$ represents the abundance of He relative to H, while $n_{\rm H}$ is the total number density of hydrogen (including both neutral and ionized species).

Equation (5) divides the 100–1000 Å wavelength range into four main regions of interest:

$$\begin{aligned}
&{\rm A}: 912 < \lambda < 1000 \quad k_{\rm eff} = 0 \\
&{\rm B}: 504 < \lambda < 912 \quad k_{\rm eff} = f({\rm H\,I}, T) k_{\rm H\,I} \\
&{\rm C}: 228 < \lambda < 504 \quad k_{\rm eff} = f({\rm H\,I}, T) k_{\rm H\,I} + A_{\rm He} f(He\,{\rm I}, T) k_{\rm He\,I} \\
&{\rm D}: 100 < \lambda < 228 \quad k_{\rm eff} = f({\rm H\,I}, T) k_{\rm H\,I} + A_{\rm He} [f({\rm He\,I}, T) k_{\rm He\,I} \\
&\qquad\qquad + f({\rm He\,II}, T) k_{\rm He\,II}]
\end{aligned} \tag{6}$$

which are defined by the absorption edges of each of the three species. Beyond 912 Å, little absorption is present and the prominence is largely optically thin. Under the assumption of ionization equilibrium, the ion fractions f are a known function of the electron temperature (e.g., Bryans et al. 2009, Dere et al. 2009 for T_e beyond 10,000 K); also, the absorption cross sections for each species are known from atomic physics (from the photoionization cross sections, e.g., Verner et al. 1996). Thus, the absorption process is dependent on three main, unknown properties of the absorbing material: its total hydrogen number density $n_{\rm H}$, its electron temperature, and its helium abundance relative to hydrogen.

The top panels of Figures 1 and 2 display $k_{\rm eff}$ as a function of temperature for the B, C, and D wavelength regimes, adopting the He/H values of 5% and 10%, respectively. The absorption cross sections have been calculated using the photoionization cross sections of Verner et al. (1996). The bottom panels show the percent contribution of each of the three ions to the total value of $k_{\rm eff}$. In Region B, absorption is only due to neutral H and as the plasma temperature rises and H ionizes, it decreases very quickly; there is no dependence on the He abundance. The temperature dependence of $k_{\rm eff}$ is very strong for $T_e \geqslant 15{,}000$ K, while it is very mild at lower temperatures where almost all hydrogen is neutral.

In Regions C and D, the presence of He absorption has two main effects on $k_{\rm eff}$: first, it introduces the dependence on the He/H relative abundance; and second, it extends the range where $k_{\rm eff}$ is weakly dependent on temperature to higher values. The latter effect is due to the fact that the ionization potential of He is larger than that of H, so that He resists ionization for a larger temperature range than H, and the fact that in region D the plasma absorption capability lost with He I ionization is replaced by He II absorption.

Figures 1 and 2 thus show that (1) the absorption properties of the slab depend on the electron temperature in different ways depending on the wavelength of the EUV incident radiation; and (2) they are fairly constant up to almost 100,000 K at wavelengths below 228 Å. Also, above $\approx$25,000 K, the slab absorption in region D is almost exclusively due to He rather than H (while in region C hydrogen becomes again important for $T > 80{,}000$ K), whereas it is only due to H at wavelengths between 504 Å and 912 Å.

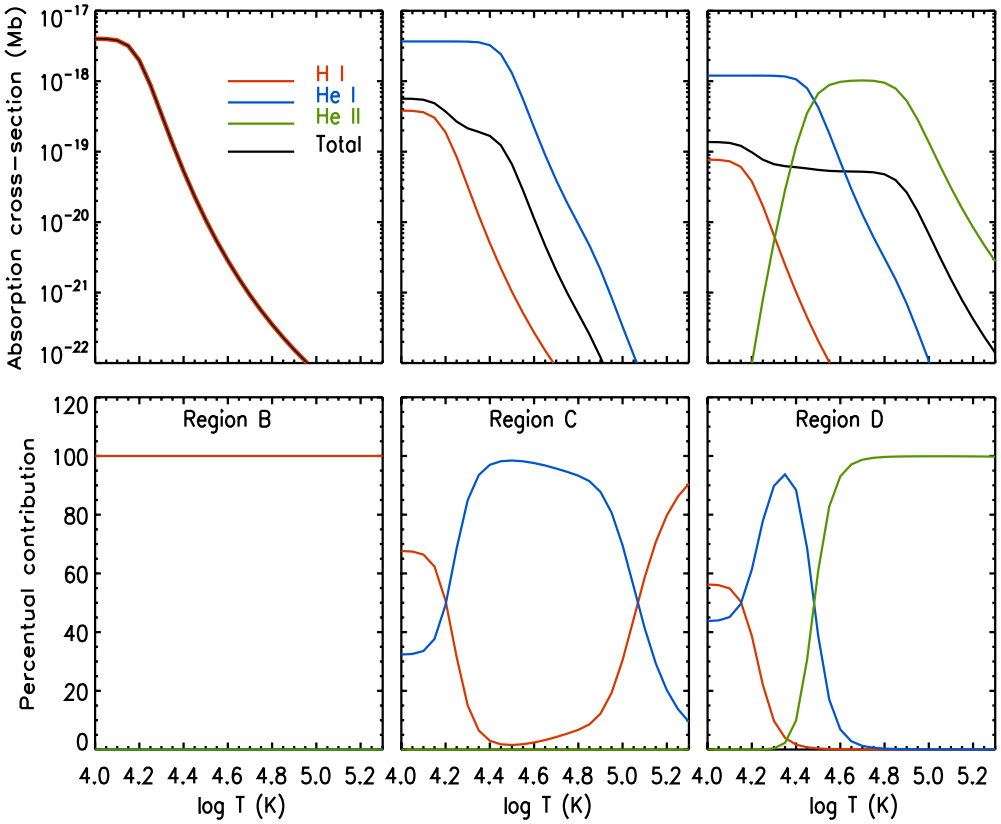

Figure 1. Top: effective absorption coefficient $k_{\rm eff}$ as a function of temperature for wavelength regions B, C, and D (defined in Table 1). The helium abundance has been assumed to be 5% of hydrogen ($A_{\rm He} = 0.05$). Red: H I; blue: He I; green: He II; black: total $k_{\rm eff}$ given by Equation (5). Bottom: percent contribution of each species to the total $k_{\rm eff}$.

(A color version of this figure is available in the online journal.)

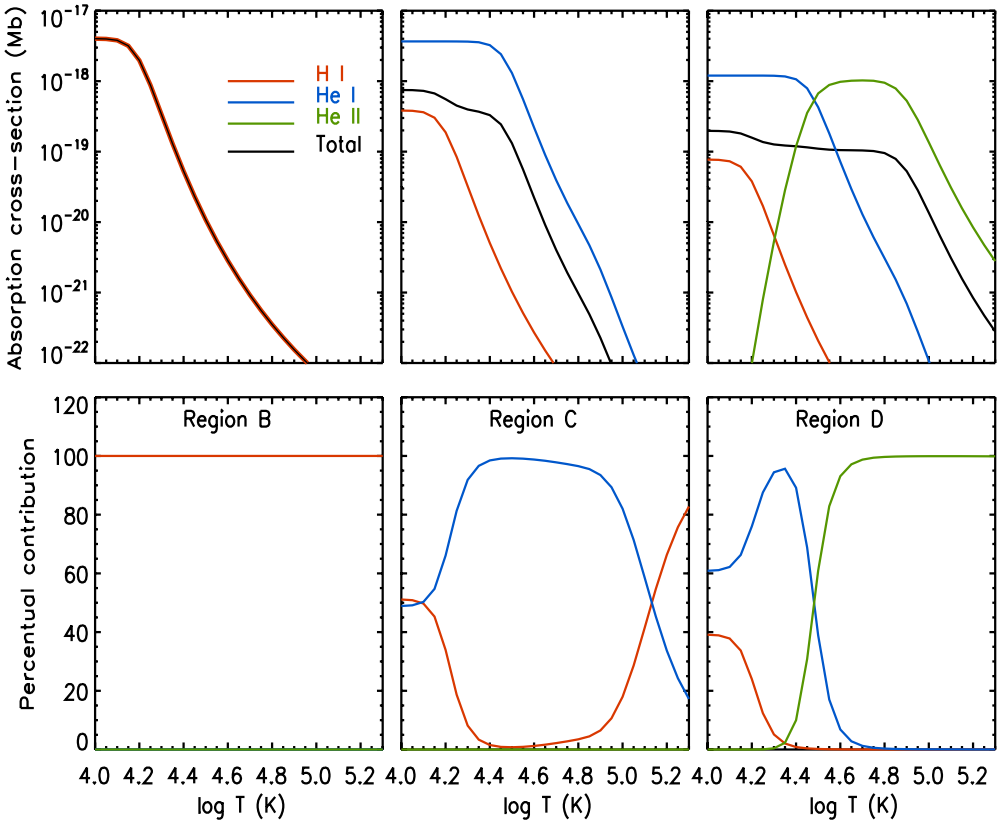

Figure 2. Same as Figure 1, with $A_{\rm He} = 0.10$.

(A color version of this figure is available in the online journal.)

Table 1
Space-borne Instruments Observing EUV Radiation in the Four Spectral Regions between 100 Å and 1000 Å Characterized by Different H I, He I, and He II Absorption Properties

Region	Wavelength Range	Spectrometer	Imager
A	$\lambda > 912$	SUMER	
B	$504 < \lambda < 912$	CDS, SUMER	
C	$228 < \lambda < 504$	CDS, EIS	EIT, EUVI, *TRACE*, AIA
D	$100 < \lambda < 228$	EIS	EIT, EUVI, *TRACE*, AIA, SWAP

2.2. EUV Absorption as a Diagnostic Tool

The diagnostic tool we propose in the present work capitalizes on the different temperature dependence of $k_{\rm eff}$ in the three different wavelength regions. In order to be applied, it requires observations at wavelengths spanning at least two of the three regions; availability of observations in all three regions further increases the possible applications. Fortunately, combinations of the available space instrumentation allows the application of these technique to existing observations of both filaments (that is, prominences observed inside the solar disk) and prominences at the limb, as shown in Table 1. Almost all instruments sample wavelengths at least in two of these three ranges.

Since the temperature effects on $k_{\rm eff}$ are most evident at temperature ranges larger than ≈15,000 K, this technique is in principle best applied to prominences whose plasma is relatively hot to begin with, or is being heated, such as in erupting prominences (e.g., Landi et al. 2010).

2.3. Basic Principle of the Diagnostic Technique

The diagnostic technique we propose relies on the determination of the coefficient $e^{-\tau}$ for many different spectral lines or narrow-band filters. Let us assume for a moment that we have been able to measure the coefficient $e^{-\tau}$ in Equation (1), for example, by determining the ratio $F_{\rm obs}/F_{\rm inc}$. We will discuss in the next section a few cases where such a measurement (or an equivalent one) can be performed. We will also further assume that the physical properties of the absorbing material are approximately the same along the path length S of the absorbing material crossed by the line of sight, and that the absorbing slab does not emit radiation at the wavelengths used. In this case, Equations (1) and (4) can be combined to give

$$\tau = k_{\rm eff}(A_{\rm He}, T) N_{\rm H} \tag{7}$$

$$\ln\left(F_{\rm obs}/F_{\rm inc}\right) = -k_{\rm eff}(A_{\rm He}, T) N_{\rm H}, \tag{8}$$

where $N_{\rm H} = \int_0^S n_{\rm H} dl$ is the hydrogen column density (in cm^{-2}). It is important to notice that both $N_{\rm H}$ and S are properties of the absorbing plasma only.

The effective absorption coefficient $k_{\rm eff}$ can be calculated as a function of temperature for any spectral line or narrow-band imaging channel once $A_{\rm He}$ has been specified. In case we have a narrow-band filter, $k_{\rm eff}$ can be easily calculated as it changes slowly with wavelength over the width of the filter itself, which usually encompasses from a few to a few tens of Å (within ≈20% in the available narrow-band imagers). This allows us to define the function

$$L(T) = -\frac{1}{k_{\rm eff}(T)} \ln\left(\frac{F_{\rm obs}}{F_{\rm inc}}\right) = \frac{k_{\rm eff}(T_{\rm abs})}{k_{\rm eff}(T)} N_{\rm H}, \tag{9}$$

where $k_{\rm eff}(T)$ is calculated as a function of temperature T using Equation (5) at the wavelength of each spectral line, and/or the central wavelength of all narrow band imagers used. We indicate with $T_{\rm abs}$ the temperature of the absorbing material. The main property of the $L(T)$ function is

$$L(T_{\rm abs}) = N_{\rm H} \tag{10}$$

for any spectral line or narrow-band imaging channel we consider. Since $N_{\rm H}$ is a property of the absorbing material only, the $L(T_{\rm abs})$ values of all the spectral lines or narrow-band filters must be the same. Equation (10) allows us to use the function $L(T)$ in the same way as the L-function defined by Landi & Landini (1997). If we measure $F_{\rm inc}$ and $F_{\rm obs}$ (or some combination of them, as we will see in the next section) for a number of spectral lines and/or narrow-band images, and plot their $L(T)$ functions in the same figure as a function of temperature, then all curves will cross the same point $(T_{\rm abs}, N_{\rm H})$. An example (discussed below) is given in Figure 3. The coordinates of the crossing point can then be used to determine both the absorbing plasma electron temperature $T_{\rm abs}$ and the $N_{\rm H}$ value; the latter can in turn be used to determine the average number density of H in the absorbing material using some assumption or estimate of the length S.

Also, the presence of a single crossing point for all curves provides a check on the main assumptions of this technique, namely, that the absorption properties of the prominence plasma are approximately the same everywhere in the prominence itself and that the absorbing plasma does not emit radiation at the wavelengths used. Also, the behavior of the $L(T_{\rm abs})$ functions of different wavelength regimes can also provide a direct determination of $A_{\rm He}$.

2.4. Example: SDO/AIA Narrow-band Images

An example of this technique is shown in Figure 3. In this figure, simulated $F_{\rm obs}/F_{\rm inc}$ ratios have been calculated at the wavelengths of a few *SDO*/AIA channels for a prominence with total $N_{\rm H} = 6.3 \times 10^{18}$ cm^{-2} and $T_{\rm abs}$ =30,000 K, assuming constant $k_{\rm eff}$ over the entire width of the filter bandpass; this corresponds to $F_{\rm obs}/F_{\rm inc}$ ratios of 0.66, 0.55, 0.56, and 0.49 for the 171 Å, 195 Å, 304 Å, and 335 Å *Solar Dynamics Observatory* (*SDO*) channels, respectively. The incident intensities were calculated using CHIANTI (Landi et al. 2013) and the quiet Sun spectrum differential emission measure (DEM). We artificially added a small amount to the $L(T)$ functions of the 195 Å and 335 Å curves to make them more easily visible in the plot (otherwise the 304 Å and 335 Å curves, as well as the 171 Å and 195 Å curves, would have been coincident). An arbitrary 20% uncertainty is associated with each curve and is shown as dashed lines in Figure 3. All channels have also been assumed to produce zero emission for simple demonstration purposes. The He/H abundance has been assumed to be $A_{\rm He} = 0.085$. The *SDO*/AIA channels sample wavelengths belonging to regions C and D, so that their $L(T)$ functions have a very different temperature dependence due to the He II absorption: as expected, their crossing point is very sharply defined and provides a rather precise measurements of $T_{\rm abs}$ and $N_{\rm H}$. On the contrary, channels whose wavelengths belong to the same spectral region provide completely overlapping $L(T)$ functions so that they cannot provide any defined crossing point. However, if their $L(T)$ functions do not overlap, then the difference between them can be used to indicate one (or a combination) of the following scenarios: (1) the presence of emission from the absorbing material itself; (2) problems in the atomic physics; (3) the possible multi-temperature structure of the absorbing prominence;

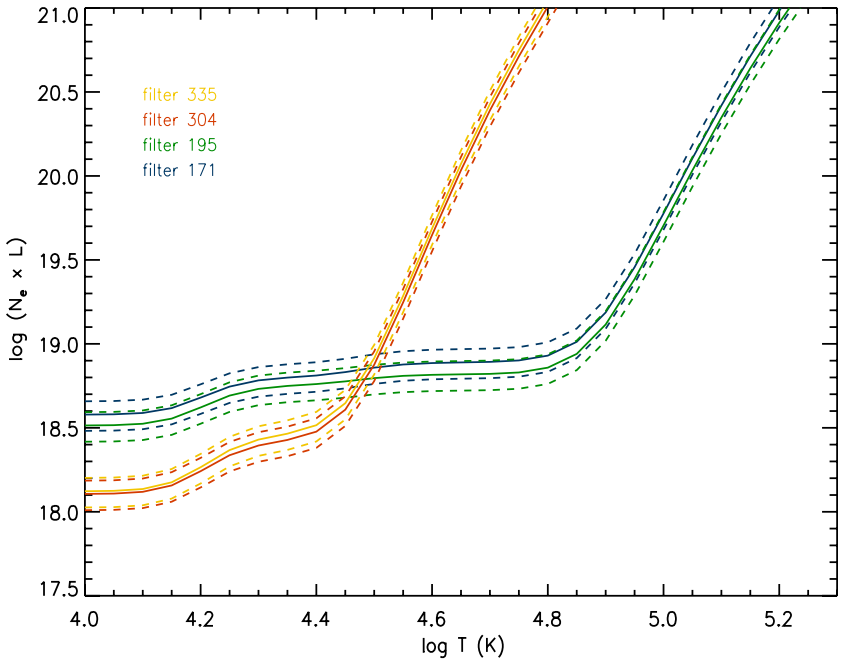

Figure 3. Example of the diagnostic technique applied to simulated intensities for four channels of the *SDO*/AIA narrow-band imagers (see Section 2.4 for details). The crossing point allows to determine the plasma temperature and column density.
(A color version of this figure is available in the online journal.)

(4) inaccuracy of the assumed $A_{\rm He}$ value used to calculate the $L(T)$ function. Discriminating between these different scenarios can be difficult, and can only be done on a case by case basis.

It is important to note that when lines or channels from only regions C and D are available, and the temperature of the absorbing slab is between ≈15–20,000 K and ≃80,000 K, only He absorption is significant so that the ordinate of the crossing point allows the direct determination the helium column density with no assumption on $A_{\rm He}$. When lines or channels from all three wavelength ranges are available and the temperature is in the 15,000–80,000 K range, the difference in height between region B $L(T)$ functions and the crossing point defined by $L(T)$ functions from C and D provides a direct measurement of $A_{\rm He}$. This measurement is very important in the case of erupting prominences as it can be compared with in-situ $A_{\rm He}$ measurements from interplanetary CMEs (ICMEs).

It is important to note that the $L(T)$ functions of each channel are defined using some types of ratios (as shown in Section 3) of the emission of the same channel, rather than its absolute values. As a consequence, the $L(T)$ values are not directly dependent on the intensity calibration of the instrument and on the temperature response function of its channels if the instrument uses narrow-band filters. Thus, an important source for uncertainty is removed.

2.4.1. Limitations of This Technique

This diagnostic technique relies on a number of assumptions that can limit its application. First, it relies on the assumed homogeneity of the absorbing plasma along the line of sight, both in terms of composition ($A_{\rm He}$) and temperature. These limitations can be severe in case this technique is applied to large portions of a prominence or filament, and can be minimized to some extent if small fields of view are selected.

The second limitation is due to the possible emission of the absorbing plasma itself. Such emission is commonly observed in the He II lines both by spectrometers and imagers, and it indicates plasma temperatures roughly in the $\log T = 5.0$ temperature regime which does not allow the use of He II spectral lines or narrow-band channels centered on the He II λ304 line. An interesting discussion of prominence emission in the He II λ256.3 line observed by EIS can be found in Labrosse et al. (2011), which clearly shows the difficulty of accounting for prominence emission in He II. Several studies have also reported non-negligible emission from the prominence-corona transition region (PCTR), which can be detected by both spectrometers and imagers. Such emission affects different lines and different narrow-band channels in different ways, due to the particular nature of the emission observed by each of them. For example, Parenti et al. (2012) have shown that significant emission is expected in the 131 Å and 171 Å channels (dominated by Fe VIII and Fe IX spectral lines) from the PCTR. The effect of this radiation should be apparent in diagnostic figures such as Figure 3, and are expected to provide a scatter in the curves that makes the identification of a crossing point more difficult.

3. APPLICATIONS OF THE TECHNIQUE

In order to utilize the properties of EUV absorption for prominence plasma diagnostics, it is necessary to first define a function $L(T)$ that has the properties described in the previous section using observed EUV line or narrow-band intensities. The easiest way to achieve this is to compare intensities measured over a prominence with their values measured near the prominence itself.

Figure 4 shows a simplified version of the geometry of the problem in the case of prominences observed against the solar disk. It is the same as in Gilbert et al. (2005). Let F_a and F_b be the measured EUV intensity values observed along the lines of sight a and b, where a intercepts a prominence while b lies close, but outside, of it. F_a and F_b can be given either by spectral line intensities or narrow-band images. Both lines of

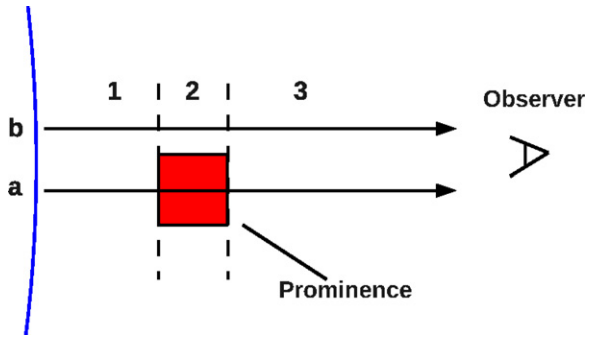

Figure 4. Cartoon showing a simplified version of the geometry discussed in Section 3, in the case of absorbing plasma observed against the solar disk. Regions 1, 2, and 3 define the "background," "prominence," and "foreground" regions, respectively, of both lines of sight *a* and *b*.

(A color version of this figure is available in the online journal.)

sight are divided in three sections, where section 1 indicates the region behind the prominence (the "background region"), section 2 corresponds to the finite length S of the prominence, and section 3 covers the entire distance between the upper boundary of the prominence and the observer (the "foreground region"). The fluxes F_a and F_b are given by

$$\begin{aligned} F_a &= F_{a1}e^{-\tau} + F_{a2} + F_{a3} \\ F_b &= F_{b1} + F_{b2} + F_{b3}. \end{aligned} \tag{11}$$

Our goal is to determine τ as a function of the two observables F_a and F_b. However, this equation has six more unknowns, namely, the background, prominence, and foreground intensities for each of the two line of sights, so that some assumptions are needed. First, our technique assumes that the absorbing plasma does not emit, so that $F_{a2} = 0$. For example, Gilbert et al. (2005) showed that the emission of the prominence itself (F_{a2}) at coronal temperatures is negligible. Also, when the selected lines of sight a and b lie close to each other, and the prominence or filament is observed far from complex plasma configurations, their foreground and background emission are likely to be similar: $F_{a1} = F_{b1} = F_1$ and $F_{a3} = F_{b3} = F_3$. Thus, the set of Equations (11) simplifies to

$$\begin{aligned} F_a &= F_1e^{-\tau} + F_3 \\ F_b &= F_1 + F_2 + F_3, \end{aligned} \tag{12}$$

where we also indicate $F_2 = F_{b2}$ for convenience of notation. Even if the geometrical configuration is different from the one shown in Figure 4, these equations also hold in the case of a prominence observed outside the solar disk, since the same approximations apply if the lines of sight a and b are chosen carefully. The only difference is given by the larger length of the line of sight of the region behind the prominence.

3.1. Special Case I

If the absorbing material is located at altitudes much larger than the scale height of the coronal emission in the solar atmosphere, like, for example, an accelerating erupting prominence during a CME onset observed against the solar disk, then the emission from the foreground and from the plasma in section 2 of the line of sight becomes negligible relative to the background emission. This is due to the fact that the plasma density at or above the absorbing material height is low. In this simplified case, $F_2 \ll F_1$ and $F_3 \ll F_1$, so that

$$\begin{aligned} \tau &= -\ln\frac{F_a}{F_b} \\ L(T) &= -\frac{1}{k_{\rm eff}(T)}\ln\left(\frac{F_a}{F_b}\right) \end{aligned} \tag{13}$$

and the diagnostic technique outlined in the previous section can be directly applied. When time series of observations are available, this technique can provide the measurement of the erupting prominence temperature as a function of time as long as the prominence is absorbing and, if enough data are available and the plasma temperature is in the right range, also of the He/H relative abundance.

3.2. Special Case II

In this case, we consider a quiescent prominence sitting at the solar limb in the absence of active regions in the foreground and background. Under this configuration, the foreground and background emission can be assumed to be roughly the same as their line of sight length and plasma physical conditions are approximately similar: $F_1 \simeq F_3$. Also, the length of the line of sight at the limb is much larger than the prominence depth S, so that F_2 can be safely assumed to be negligible even if the prominence is close to the limb. Simple algebraic considerations allow us to rewrite Equations (11) as

$$\begin{aligned} \tau &= -\ln\left(2\frac{F_a}{F_b} - 1\right) \\ L(T) &= -\frac{1}{k_{\rm eff}(T)}\ln\left(2\frac{F_a}{F_b} - 1\right) \end{aligned} \tag{14}$$

and apply the diagnostic technique described in the previous section to the $L(T)$ functions.

3.3. General Case

Equations (12) have two observables and four unknown quantities, so that some assumptions (or more observables) are needed. To deal with this case, we follow the same approach as Gilbert et al. (2005). They considered a configuration where two very close parts of the prominence were observed against two very different backgrounds, and assumed that the coefficient $e^{-\tau}$ is the same in both locations. This configuration is very easily obtained when the same prominence is observed across the solar limb, so that a portion of the prominence can be studied on the disk (we will call this position D), and another portion lies outside the limb (position L).

Gilbert et al. (2005) further assumed that (1) F_2 was proportional to the foreground intensity F_3, so that $F_2 = \gamma F_3$ everywhere in the proximity of the prominence, and (2) that the foreground emission of the D and L regions has a constant ratio $F_3^D/F_3^L = \beta$. Under these assumptions, we have four different observables:

$$\begin{aligned} F_a^L &= F_1^L + (\gamma+1)F_3^L \\ F_b^L &= F_1^Le^{-\tau} + F_3^L \\ F_a^D &= F_1^D + \beta(\gamma+1)F_3^L \\ F_b^D &= F_1^De^{-\tau} + \beta F_3^L, \end{aligned} \tag{15}$$

where F_a^D, F_b^D, F_a^L, and F_b^L are observed from spectrally resolved emission line or narrow-band filter images. Simple

algebraic consideration allows us to estimate the coefficient $e^{-\tau}$ as

$$e^{-\tau} = \frac{F_b^L - \beta F_b^D}{F_a^L - \beta F_a^D}. \quad (16)$$

The advantage of Equation (16) is that it requires only the estimation of the constant β and not of γ. Gilbert et al. (2005) determined β assuming that the path length difference between positions L and D was negligible so that the only difference between the two positions was due to the intensity falloff with distance from the limb, which can be easily determined from the observations themselves.

Equation (16) can be applied to any spectral line or narrow-band image for which two positions L and D can be selected, so that

$$\tau = -\ln\left(\frac{F_b^L - \beta F_b^D}{F_a^L - \beta F_a^D}\right)$$
$$L(T) = -\frac{1}{k_{\rm eff}(T)} \ln\left(\frac{F_b^L - \beta F_b^D}{F_a^L - \beta F_a^D}\right) \quad (17)$$

and the diagnostic technique can be applied.

4. APPLICATION TO AIA DATA

4.1. Observations and Measurements

In order to be applied successfully, this technique requires data that span at least two of the wavelength domains listed in Table 1. We have chosen to demonstrate this technique by applying it to AIA observations of a CME described by Innes et al. (2012). In this event, occurred immediately after a flare at 6:00 UT on 2011 June 7, a CME erupted close to the west limb; during the take-off of the CME plasma, several small and cold plasma blobs reached a certain height above the limb, but then stopped accelerating and fell back on the Sun. Before falling on the solar photosphere, AIA observed their trajectory above the solar disk: since the plasma in these plasma blobs was cold, they could be observed in absorption. We focus on two different portions of one of these plasma blobs, and we will study the effects of absorption at two different moments during the eruption: 07:03 UT and 07:51 UT. The plasma blob had been initially accelerated away from the Sun in a direction toward the Earth, and later fell back on the Sun: the positions of this blob relative to the Sun and the observer are shown in Figure 5, where the red and green portions of the line of sight indicate the background and foreground regions, respectively. The image of the plasma blob taken at 07:03 UT is shown in Figure 6 in all AIA bands, taken at 07:03 UT. The plasma blob is almost invisible at 94 Å and becomes increasingly darker as the wavelength increases. The height of the plasma blob above the photosphere was large enough to allow us to neglect the emission of the plasma in front of the plasma blob for all channels, so that the diagnostic technique could be applied following the guidelines of Special Case I.

We have used AIA synoptic observations with a cadence of three minutes. We have applied the diagnostic technique to the portion of the plasma blob indicated by the crossing of the vertical and horizontal lines in Figure 6, and F_a was determined summing the observed intensity in each channel over the selected area. The intensity F_b can be determined in two ways: either averaging the intensity of adjacent pixels to the selected area, or using the light curve of the selected area itself. Figure 6 shows that the selected pixels are located very close to the limb as seen from Earth, so that limb brightening causes large local variations of the intensity of the adjacent pixels, making it difficult to provide an estimate of the emission behind the plasma blob. An inspection of the light curves of the selected area showed that once the passage of the absorption feature is excluded, the intensity of each of the AIA channels was evolving smoothly with time, with no sudden brightening. A separate linear fit has been made to the light curves of each channel (since each of them was evolving differently from the other) and the intensity expected at the time of the plasma blob passage has been estimated from the fit coefficients.

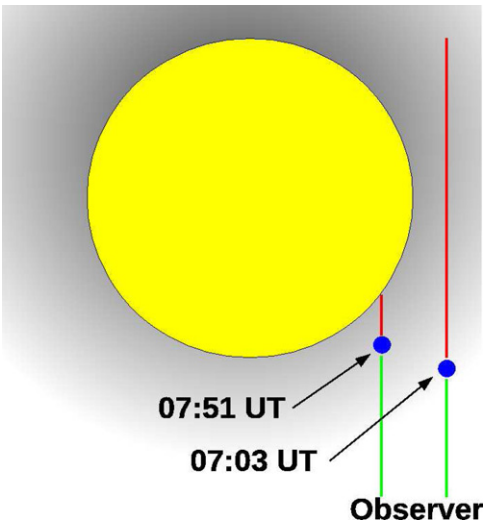

Figure 5. Cartoon showing the position of the fragment of the CME eruption of 2011 June 7 used to demonstrate the plasma diagnostic technique. The Sun is shown as observed from the north pole. The two blue circles correspond to the positions of the fragment at 07:03 UT and 07:51 UT. The green and red sections of the two lines of sight indicate the portion of the coronal plasma in front and behind the fragment, respectively. The radial gray shading of the corona indicates the decrease of the coronal emission with distance.

(A color version of this figure is available in the online journal.)

4.2. Results

The results of the application of the technique are shown in Figure 7. This figure displays the curves of all AIA channels. The fact that the 304 Å and 335 Å channels belong to a different wavelength region than the others enabled us to measure the column density and the temperature of the plasma blob itself from the crossing of all curves to be $3.6^{+1.1}_{-0.7} \times 10^{19}$ cm^{-2} and 33,100 $\pm$ 2200 K, respectively, assuming that the helium abundance is 5% of hydrogen. The most important thing to notice in Figure 7 is that the crossing point is extremely well defined, and it allows a very accurate diagnostics of the absorbing plasma temperature and column emission measure. The crossing region is marked by the horizontal and vertical dot-dashed lines. The $L(T)$ curve of the 131 Å channel is slightly larger than all others, but the discrepancy is within uncertainties.

It is interesting to note that the large uncertainty in the absorption ratio given by the 94 Å channel (whose absorption is almost invisible in Figure 6) is amplified in the diagnostic technique due to the non-linear propagation of the uncertainties, and makes this channel almost useless for this type of diagnostics (despite the excellent agreement of the actual L function value). The $L(T)$ function of this channel is shown in Figure 7 only for the sake of completeness.

The determination of the column density allows us to make some crude determination of the plasma electron density, by

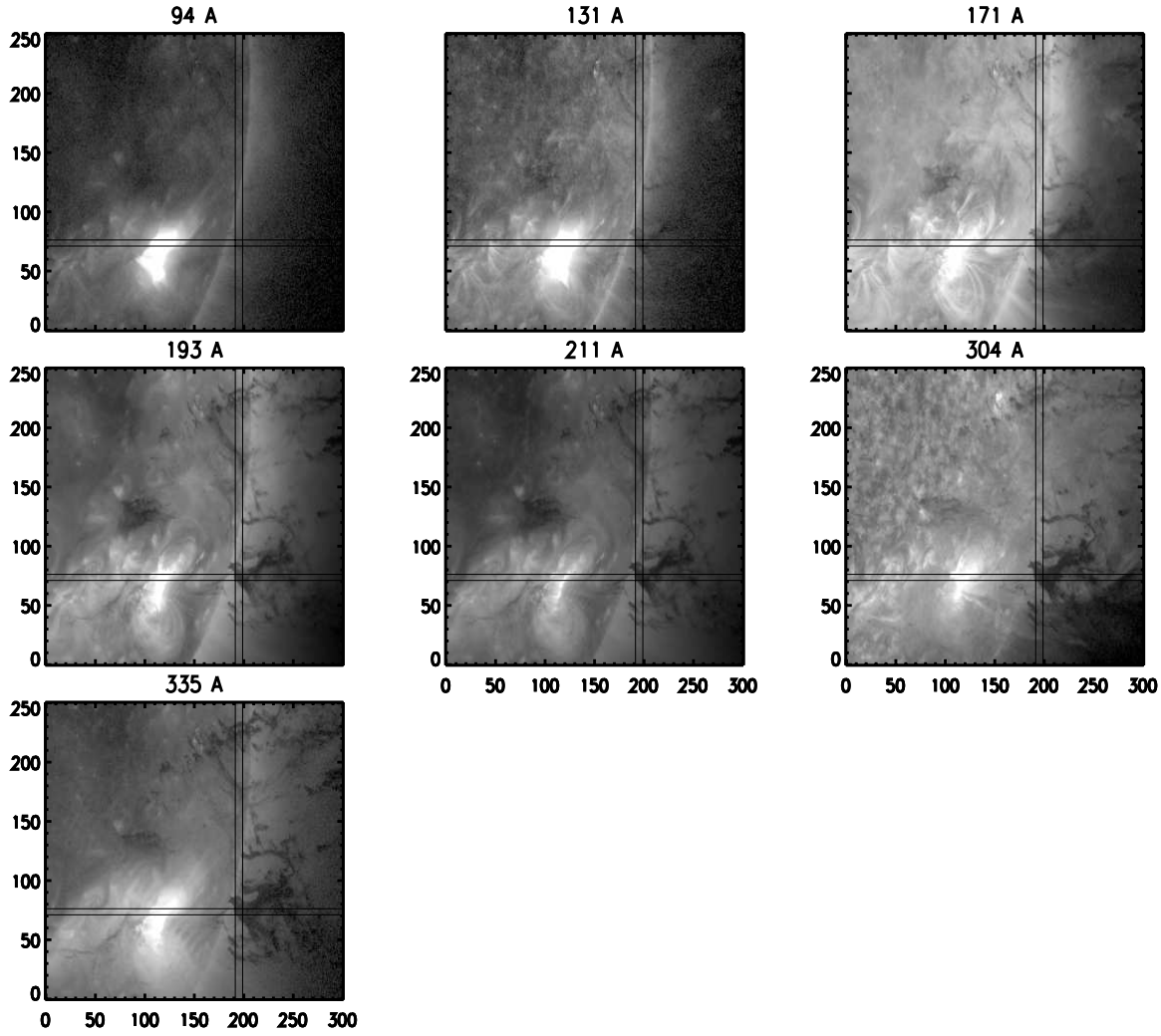

Figure 6. AIA images of the plasma fragment falling back on the Sun following the CME event of 2011 June 7. This image was taken at 07:03 UT. The portion of the plasma blob selected for analysis is marked by the crossing of the horizontal and the vertical lines.

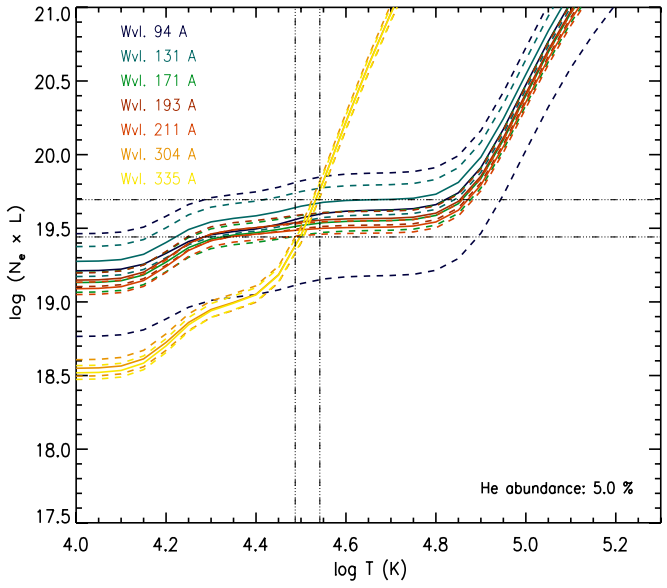

Figure 7. Diagnostic technique applied to the selected plasma blob shown in Figure 6, using the absorption ratios of all the AIA channels. The horizontal and vertical dash-dotted lines show an estimate of the crossing region.

(A color version of this figure is available in the online journal.)

making some assumption of the plasma filling factor and the dimension D of the absorbing parcel of plasma along the line of sight. The dimensions of the rectangular area selected in Figure 6 are $L_X \approx 7000$ km and $L_Y \approx 5300$ km along the solar X and Y dimensions, respectively: we have somewhat arbitrarily assumed $D = 6000$ km. Also, we further assumed a unity filling factor. By using the assumption that the plasma in the absorbing parcel is approximately homogeneous, we can derive the neutral hydrogen density from

$$N_{\rm H} = \int_0^D n_{\rm H} dl \approx \langle n_{\rm H} \rangle D, \tag{18}$$

where $\langle n_{\rm H} \rangle$ is an estimate of the average total hydrogen density. Using the crossing point in Figure 7, $\langle n_{\rm H} \rangle = 6.0^{+1.8}_{-1.2} \times 10^{10}$ cm^{-3}. Calculating the ratio of neutral hydrogen to free electrons in a plasma using the CHIANTI software, the electron density is $n_e = 6.5^{+1.9}_{-1.3} \times 10^{10}$ cm^{-3}. Given the assumption of unity filling factor, this estimate of the hydrogen density is in reality a lower limit. These results are in broad agreement with the estimates of $N_{\rm H}$ and $\langle n_{\rm H} \rangle$ provided by Williams et al. (2013) from a different fragment of the same erupting prominence, even though the method followed by these authors is different from ours and provides only a lower limit to the column density and no information on the absorbing plasma temperature.

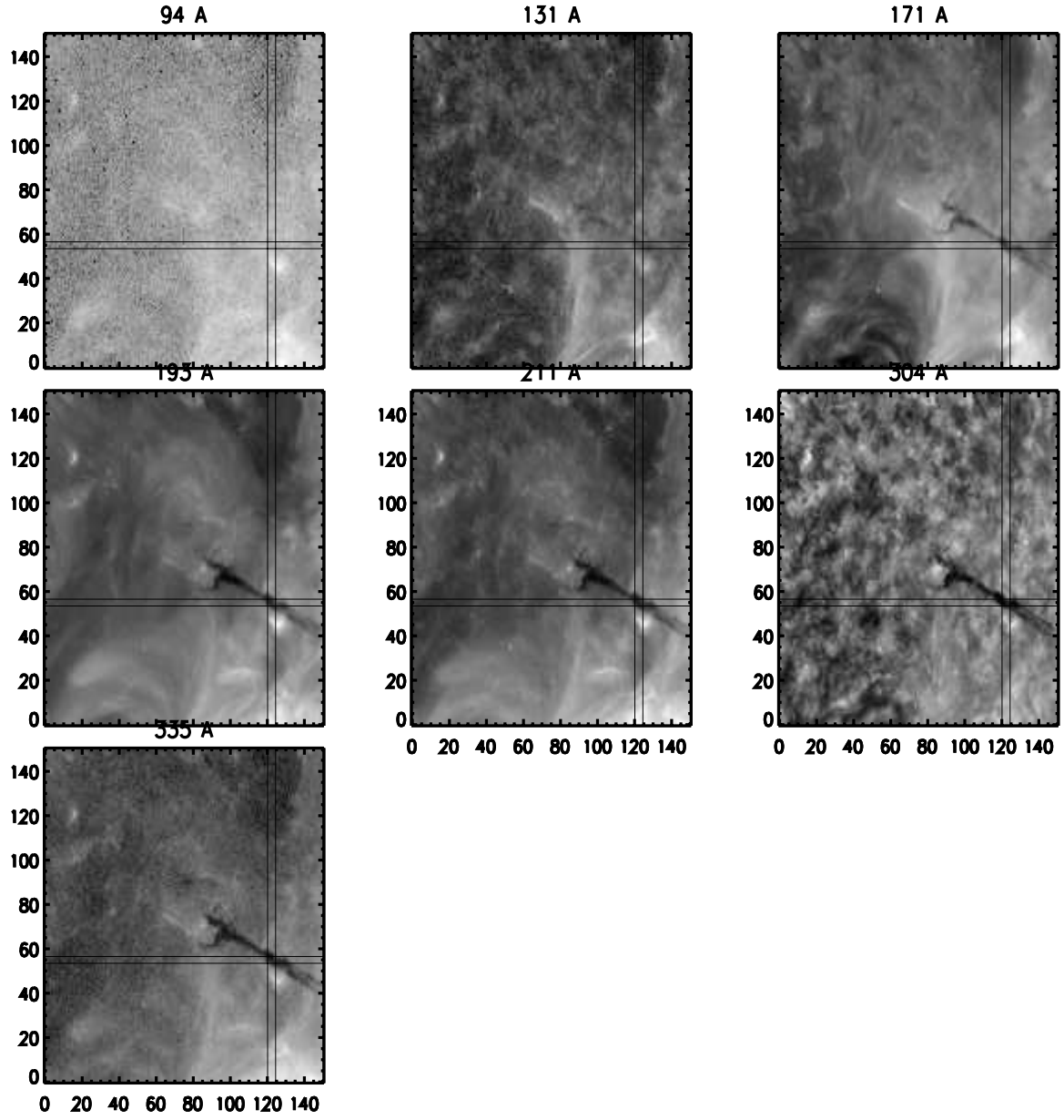

Figure 8. Same as Figure 6, taken at 07:51 UT. The plasma blob is now significantly closer to the solar surface. The portion of the plasma blob selected for analysis is marked by the crossing of the horizontal and the vertical lines.

We have also applied the same technique to another portion of the blob observed at 07:51 UT, also shown in Figure 5. It is important to note that the amount of coronal plasma located between this blob and the observer is much larger at 07:51 UT than at 07:03 UT, because the blob is traveling away from the observer: we expect that the foreground emission will be more important in this case. Figure 8 shows the absorption in all AIA channels and the portion of the absorbing plasma we selected for analysis. At this time, the fragment is located at a much lower height than the fragment in Figure 6. The application of the diagnostic technique is shown in Figure 9. The curves of the 193 Å and 211 Å channels in Figure 9 are lower than the common crossing point, mostly defined by 131 Å, 171 Å, 304 Å, and 335 Å, and also disagree with each other. This disagreement is discussed in the next section; however, we note that even considering this significant disagreement, the uncertainty introduced on the plasma temperature and column density by the lack of a common crossing point is limited, as the temperature and column density do not change much. In fact, using the crossing point provided by all curves except the 193 Å and 211 Å channels, the temperature and the column density of this fragment are comparable to those of the previous example: 34,500 $\pm$ 3000 K and $3.5^{+1.1}_{-0.7} \times 10^{19}$ cm^{-2}, respectively. When including those two channels, these values become 33,100 $\pm$ 4700 K and $2.3^{+2.0}_{-1.3} \times 10^{19}$ cm^{-2}: the uncertainties have grown larger, but both quantities are still fairly well determined.

5. DISCUSSION

5.1. Emission in the 304 Å Channel

The $L(T)$ curves of the 304 Å channel in Figures 7 and 9 almost perfectly overlap with those of the 335 Å channel, indicating that there is very little He II emission in the plasma blob, despite the electron temperature being very close to the abundance peak of that ion. The reason for such a low He II emission is the low temperature of the plasma blob itself, which

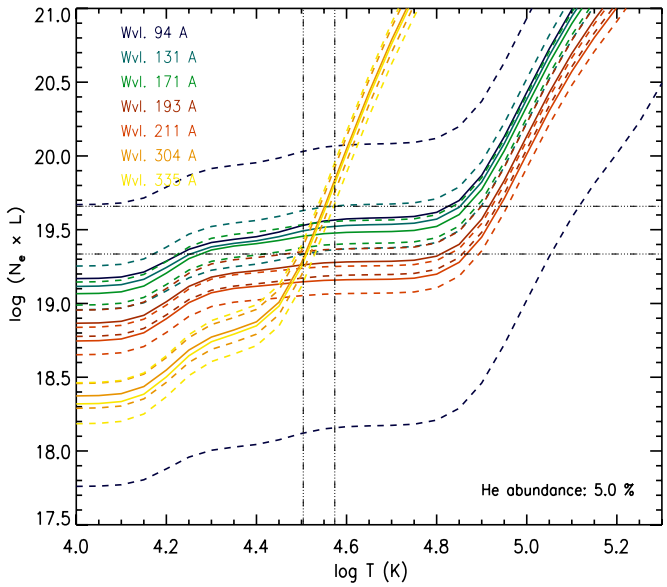

Figure 9. Same as Figure 7, for the dataset observed at 07:51 UT. The horizontal and vertical dash-dotted lines show an estimate of the crossing region.

(A color version of this figure is available in the online journal.)

makes collisional excitation of the He II Lyα lines at 304 Å rather inefficient even though the fractional abundance of this ion is expected to exceed 50%. In order to check that the plasma blob emission in the 304 Å channel is indeed negligible, we have determined an upper limit to the fragment's emission in the He II Lyα by assuming that it is optically thin, even though radiative transfer is likely to be significant. We have assumed that the plasma blob DEM $\varphi(\log T)$ is Gaussian in $\log T$ space, with peak temperature given by the temperature measured from Figure 7, width given by $\sigma = 0.05$ (also in $\log T$), and an amplitude chosen so that total emission measure is given by

$$\int_0^\infty \varphi(\log T) d\log T = n_e^2 L_X L_Y D. \quad (19)$$

The plasma blob spectrum has been calculated and folded through the AIA effective area, and the resulting count rates were $\simeq$0.04 DN s^{-1} for the 304 Å channel and smaller than 1.5×10^{-4} DN s^{-1} for all other channels. Radiatively excited contributions from the He II λ303.7 spectral feature were found to be negligible. Even considering the large uncertainties in such an estimation, the calculated count rates are much lower than the observed ones in the absorbing plasma parcel, which are around 200 DN s^{-1} for the 304 Å channel, and thus even lower when relaxing our crude assumptions.

We made some tests experimenting with the width of $\varphi(\log T)$ and found that it has little effect on the predicted count rates. On the contrary, increasing the temperature makes the collisional excitation of the He II Lyα line more efficient, so that in the $\log T = 4.8$–5.1 range the emission reaches the 16.5–47.1 DN s^{-1}, which is not negligible anymore. However, Figure 7 clearly shows that those temperatures are way too far from the crossing point to pose any problem.

In any case, even if the 304 Å channel could not be used, the diagnostic technique can still be applied using the 335 Å channel, which is not affected by significant cold emission.

5.2. The 195 and 211 Å channels

The 195 and 211 Å channels show a lower L function value beyond uncertainties in Figure 9. At the temperature given by the crossing point of all the other lines, the ratio of the $L(T)$ functions of the 193 Å and 211 Å curves to the crossing point is 0.69 ± 0.14 and 0.51 ± 0.10, respectively, indicating a factor approximately two of difference.

The fact that these two channels provide a lower $L(T)$ function value can be due to several reasons. In fact, the disagreement suggests that either the background flux or the effective absorption coefficient we used are overestimated. To understand this behavior, we have checked the effect of a number of factors on the observed intensity measurement and the effective absorption coefficient $k_{\rm eff}$ calculation.

5.2.1. Background Subtraction

First, the light curves we used to determine the background emission allow an easy linear fit to the intensities measured in these two channels before and after the passage of the absorbing plasma blob. Unless a sudden decrease in the background emission and subsequent increase to previous values occurred in both channels within the three minutes occurring between the observations we used and the neighboring ones, uncertainties in background determination do not appear to be a factor.

5.2.2. Additional Absorption Contributions

A second possible reason can be found in the calculation of the effective absorption coefficient. At the temperatures shown in Figures 7 and 9, the effective absorption coefficient is dominated by He I and He II: the photoionization cross sections we used for He I were taken by Verner et al. (1996) from very accurate laboratory measurements (Samson et al. 1994), while the Verner et al. (1996) values for He II were corrected by us to match the laboratory measurements of Andersen et al. (2001); we note that the laboratory measurements of Bizau et al. (2005) are in very good agreement with Andersen et al. (2001). So the uncertainty in these cross-sections is likely not the cause of the disagreement.

The method we used to calculate the effective absorption coefficient assumes that all H I, He I, and He II species are in the ground level, that is, the metastable level population is negligible. We used CHIANTI to test this assumption, and found that metastable level populations were well below the 1% level at the temperatures considered here. Also, the emission spectrum in the ranges covered by the effective areas of the 193 Å and 211 Å channels does not include any significant line emission at the temperatures indicated by Figure 7, so that the "zero-emission" approximation holds for the absorbing plasma blob.

There is the possibility that the 193 Å and 211 Å channels have no problems, and that the 93 Å, 131 Å, and 171 Å channels are the source of the disagreement, either because of an underestimated $k_{\rm eff}$ or through plasma blob emission.

We first tested for the presence of additional neutrals/ions whose recombination continuum edge falls between the 171 Å and the 195 Å channel, which contribute to the effective absorption coefficient of the 93 Å, 131 Å, and 171 Å channels. There are a few species whose recombination edges fall between 171 Å and 195 Å, whose elemental abundance makes them suitable candidates: O III, Ca IV, and C V. However, these ions provide significant increases to the effective absorption coefficient (around a factor $\approx$2) at temperatures larger than $\log T = 5.0$, so that they are not a factor in the present case.

5.2.3. Absorption Coefficient Variation

In the present work, we have calculated the effective absorption coefficient at the nominal wavelength of each of the AIA

channels, neglecting both the variation of the effective absorption coefficient itself with wavelength over the width of each AIA channel, and the possibility that the incident emission in these channels is dominated by lines far from the channel's nominal wavelength. To test these possibilities, we calculated the expected incident spectrum with CHIANTI assuming both quiet Sun and active region conditions, folded them through the AIA channels, and determined which spectral lines were providing the majority of the observed counts. In all cases, the wavelength dependence of the effective absorption coefficient is a negligible factor in the problems of the 193 Å and 211 Å channels.

5.2.4. Additional Emission Along the Line of Sight

The crossing point shown in Figure 7 is made possible by the absence of significant emission in front of the infalling fragment as well as from the plasma volume occupied by the fragment itself. However, in the particular case of this event, such assumptions do not hold any longer after the fragment has fallen to much lower heights over the photosphere, where the corona is denser and its emission cannot be neglected any more.

In this case, each of the AIA channels responds to the presence of emitting plasma at coronal temperature in a different way, depending on its particular sensitivity to different temperature ranges. In this case, the diagnostic technique we have developed cannot be applied with the approximations required by Special Case I applied above. However, it can still provide valuable information. The fragment shown in Figures 8 and 9 is an example.

In this case, there is no single crossing point which includes all the $L(T)$ curves; rather, there is a crossing point that groups all AIA channels, marked by the horizontal and vertical dot-dashed lines, except the 193 Å and 211 Å, while these two channels provide lower values of the column density. The reason is due to the fact that the fragment is traveling through the quiet Sun corona. The quiet corona plasma was shown to be almost isothermal by a number of authors (see the review of Feldman & Landi 2008 and references therein), with a temperature of $\approx 1.4 \times 10^6$ K. At these temperatures, the AIA channels which are expected to be most affected by the plasma in front of the fragment are indeed the 193 Å and 211 Å ones, while the others are sensitive either to larger or lower temperatures. This explains why all AIA channels provide a common crossing point, with the only exception of the 193 Å and 211 Å ones. Also, the crossing point of all other channels allows us to estimate the temperature and the column density of the absorbing fragment.

The question is, can the amount of disagreement of the 193 Å and 211 Å channels be used to infer some properties of the absorbing plasma? Geometrical considerations justify the assumption that the emission observed by these two channels can be approximated by Equation (12), and the temperature of the absorbing plasma ensures that it does not emit radiation that is observable by the 193 Å and 211 Å channels. However, knowledge of the fragment's $N_{\rm H}$ and T allows us to determine τ and $k_{\rm eff}$, so that we are left with three unknowns: F_1, F_2, and F_3.

Simple algebraic considerations allow us to express the difference ΔL in the value of the $L(T)$ functions of each of the 193 Å and 211 Å channels from the value $L_{\rm cross}$ of the crossing point of all other channels for which Special Case I applies as

$$L_{193,211} - L_{\rm cross} = \Delta L = -\frac{1}{k_{\rm eff}} \ln\left(\frac{1+\frac{F_3}{F_1}e^{\tau}}{1+\frac{F_2+F_3}{F_1}}\right). \quad (20)$$

Table 2
Additional Diagnostic Results for the Absorbing Fragment Observed at 7:51 UT on 2011 June 7: Upper Limit to the Thickness D of the Fragment, and Lower Limit to Its Electron Density

Channel	He/H = 2%	He/H = 5%	He/H = 10%
	Fragment thickness D (km)		
193 Å	19,500	49,000	98,000
211 Å	25,000	62,000	125,000
	Fragment electron density (cm^{-3})		
193 Å	1.5×10^{10}	6.0×10^9	3.0×10^9
211 Å	1.2×10^{10}	4.7×10^9	2.3×10^9

Note. See text for details.

The sign of ΔL depends on the relative magnitude of the terms $F_3 e^{\tau}$ and $F_2 + F_3$. In particular,

$$\begin{aligned} \Delta L > 0 &\rightarrow F_2 > F_3(e^{-\tau} - 1) \\ \Delta L < 0 &\rightarrow F_2 < F_3(e^{-\tau} - 1). \end{aligned} \quad (21)$$

If we make the assumption that the upper corona is both isothermal (with temperature $T_{\rm cor}$) and in hydrostatic equilibrium, then the intensity observed from Earth can in general be expressed as

$$F = \int_0^{\infty} N_e^2 G(T) dh \approx N_e^0 G(T_{\rm cor}) \frac{H}{2} \int_0^{\infty} e^{-x} dx, \quad (22)$$

where H is the scale height and N_e^0 is the density at the base of the corona. The expression in Equation (22) can be broken down in three terms, each corresponding to the length of the line-of-sight path corresponding to F_1, F_2, and F_3 as shown in Figure 4. If we indicate with h_1 and h_2 the bottom and the top locations of the absorbing plasma, so that $h_2 - h_1 = D$, then Equations (21) allow to determine the lower or upper limit of the thickness D of the absorbing fragment:

$$\begin{aligned} \Delta L > 0 &\rightarrow D > \frac{H}{2}\tau \\ \Delta L < 0 &\rightarrow D < \frac{H}{2}\tau. \end{aligned} \quad (23)$$

Assuming that the electron temperature of the corona is $T_{\rm cor} = 1.4 \times 10^6$ K (Feldman & Landi 2008) and a mean particle mass of $0.61 \times m_{\rm H}$, with $m_{\rm H}$ being the hydrogen mass, the results of Figure 9 indicate $\Delta L < 0$, and thus allow us to place an upper limit to the fragment's size D along the line of sight. This can in turn be combined with the value of the column density $N_{\rm H}$ and an estimate of the electron-to-hydrogen ratio from CHIANTI to provide a lower limit on the electron density, again assuming that the absorbing plasma is isothermal at the temperature indicated by the crossing point of the $L(T)$ functions. Our results are shown in Table 2; the lower limit on the electron density is also dependent on the He abundance, so that we have listed the results obtained with three values of He/H: 2%, 5%, and 10%.

6. CONCLUSIONS

The diagnostic technique that we have developed in this work can be very useful in several occasions. Below $\simeq$15,000 K, the effective absorption coefficient does not depend on the temperature, so that the availability of lines in different spectral regions can provide an estimate of the He abundance relative to

H (A_{He}) even without knowledge of the thermal properties of the prominence itself.

For hotter prominences, different combinations of observations in the 3 spectral regions where absorption of different species is dominant can provide very precise temperature estimates, along with He/H and N_H determinations. These properties are most important in studies of erupting prominences, where the prominence plasma is heated to temperatures 10 or more times the typical quiescent values, and knowledge of the temporal evolution of the temperature can provide vital constraints to models of CME acceleration and heating. Also, measurements of A_{He} can provide a direct, quantitative link between remote observations of erupting prominences near the Sun and in-situ measurements of the properties of prominence plasmas in the core of ICMEs. In all cases, care needs to be taken in checking that the emission from the plasma blob itself is minimized.

There are two main advantages in using this method. First, the solar structures that can be studied with our technique can be easily identified and studied for long periods of time, especially when images from several channels at different wavelengths are available. Second, the diagnostic technique itself is very fast and easy to apply to large datasets, so that it allows rapid and accurate measurements of column density and plasma temperature as a function of time over extended areas. This makes this technique ideal both to study individual filaments and CME events, as well as to make systematic surveys on the physical properties of many events. Also, if a reasonable assumption or estimate on the geometry of the absorbing plasma can be made, then this method provides a direct and relatively accurate measurement of the plasma hydrogen and electron density.

We have discussed the main limitations of this technique, namely, the presence of composition and thermal inhomogeneities in the absorbing plasma, as well as the emission of the absorbing plasma itself in one or more of the spectral lines/narrow-band channels currently available. We demonstrated the technique on AIA observations of EUV absorption of parcel of plasma falling on the Sun following a CME eruption, and discuss both the diagnostic capabilities of this technique.

The present diagnostic technique can be applied to data from all the recent and current space missions, such as *SOHO*, *TRACE*, *STEREO*, *Hinode,* and *SDO*, and to future ones such as Solar-C, Solar Orbiter, and Solar Probe.

The work of E.L. is supported by the NNX11AC20G and NNX10AQ58G NASA grants, and by NSF grant AGS-1154443. Fabio Reale acknowledges support from Italian Ministero dell'Universitá e Ricerca and from Agenzia Spaziale Italiana (ASI), contract I/015/07/0. The authors warmly thank the referee for comments that considerably helped us to improve the original manuscript.

REFERENCES

Andersen, P., Andersen, T., Folkmann, F., et al. 2001, JPhB, 34, 2009
Batchelor, D. A., & Schmahl, E. J. 1994, in Solar Dynamic Phenomena and Solar Wind Consequences, ed. J.J. Hunt (ESA SP-373; Noordwijk: ESA), 203
Bizau, J.-M., Champeaux, J.-P., Cubaynes, D., et al. 2005, A&A, 439, 387
Bryans, P., Landi, E., & Savin, D. W. 2009, ApJ, 691, 1540
Dere, K. P., Landi, E., Young, P. R., et al. 2009, A&A, 498, 915
Feldman, U., & Landi, E. 2008, PhPl, 15, 056501
Gilbert, H., Kilper, G., Alexander, D., & Kucera, T. A. 2011, ApJ, 727, 25
Gilbert, H. R., Holzer, T. E., & MacQueen, R. M. 2005, ApJ, 618, 524
Gilbert, J. A., Lepri, S. T., Landi, E., & Zurbuchn, T. H. 2012, ApJ, 751, 20
Golub, L., Bookbinder, J., DeLuca, E., et al. 1999, PhPl, 6, 2205
Gruesbeck, J. R., Lepri, S. T., & Zurbuchen, T. H. 2012, ApJ, 760, 141
Gruesbeck, J. R., Lepri, S. T., Zurbuchen, T. H., & Antiochos, S. K. 2011, ApJ, 703, 103
Innes, D. E., Cameron, R. H., Fletcher, L., Inhester, B., & Solanki, S. K. 2012, A&A, 540, 10
Kucera, T. A., Andretta, V., & Poland, A. I. 1998, SoPh, 183, 107
Labrosse, N., Heinzel, P., Vial, J. C., et al. 2010, SSRv, 151, 243
Labrosse, N., Schmieder, B., Heinzel, P., & Watanabe, T. 2011, A&A, 531, A69
Landi, E., Gruesbeck, J. R., Lepri, S. T., & Zurbuchen, T. H. 2012, ApJ, 750, 159
Landi, E., & Landini, M. 1997, A&A, 327, 1230
Landi, E., Raymond, J. C., Miralles, M. P., & Hara, H. 2010, ApJ, 711, 75
Landi, E., Young, P. R., Dere, K. P., Del Zanna, G., & Mason, H. E. 2013, ApJ, 763, 86
Lepri, S. T., & Zurbuchen, T. H. 2010, ApJ, 723, 22
Orrall, F. Q., & Schmahl, E. J. 1976, SoPh, 50, 365
Parenti, S., Schmieder, B., Heinzel, P., & Golub, L. 2012, ApJ, 754, 66
Samson, J. A.R., He, Z. X., Yin, L., & Haddad, G. N. 1994, JPhB, 27, 887
Tandberg-Hanssen, 1995, The Nature of Solar Prominences (Dordrecht: Kluwer)
Verner, D. A., Ferland, G. J., Korista, K. T., & Yakovlev, D. G. 1996, ApJ, 465, 487
Williams, D. R., Baker, D., & van Driel-Gesztelyi, L. 2013, ApJ, 764, 165